nature physics

SUPPLEMENTARY INFORMATION

DOI: 10.1038/NPHYS1885

Supplementary information for 'Photon shell game in three-resonator circuit quantum electrodynamics'

Matteo Mariantoni[1,3,*], H. Wang[1], Radoslaw C. Bialczak[1], M. Lenander[1], Erik Lucero[1], M. Neeley[1], A. D. O'Connell[1], D. Sank[1], M. Weides[1], J. Wenner[1], T. Yamamoto[1,3], Y. Yin[1], J. Zhao[1], John M. Martinis[1,†] and A. N. Cleland[1,‡]

[1]Department of Physics, University of California, Santa Barbara, California 93106-9530, USA
[2]Green Innovation Research Laboratories, NEC Corporation, Tsukuba, Ibaraki 305-8501, Japan
[3]California NanoSystems Institute, University of California, Santa Barbara, California 93106-9530, USA
[*]e-mail: matmar@physics.ucsb.edu
[†]e-mail: martinis@physics.ucsb.edu
[‡]e-mail: anc@physics.ucsb.edu

last updated: November 16, 2010

In this supplementary information, we provide further insight into the transduction fidelity of microwave one- and two-photon Fock states between three coplanar wave guide resonators. We provide details on the sequence used to shuffle the superposition state $|0\rangle + |1\rangle$ between two resonators, as well as explain the figures of merit we used for the transfer fidelity. In addition, we show that the exponential decay of the two-resonator vacuum Rabi swaps fits very well with a simple harmonic-mean decay model, where both the qubit and resonator energy relaxation times contribute to the effective decay of the two-resonator dynamics. Our model is confirmed by Lindblad-type numerical simulations. Finally, we explain the procedure used to correct for measurement errors and show a typical qubit visibility experiment.

1 The chip

In order to realize three-resonator circuit quantum electrodynamics (QED) experiments, a complex architecture must be designed and fabricated on a single chip. In the main text (cf. Fig. 1a) we display a photograph of the sample attached to an aluminum sample holder. The main circuit elements comprise three coplanar wave guide resonators and two superconducting phase qubits. Figure Supplementary 1 shows a detail of qubit Q_1, together with its readout d.c. superconducting quantum interference device (SQUID), control and readout lines and the coupling capacitors to resonators $\mathrm{R_a}$ and $\mathrm{R_b}$, $C_{1\mathrm{a}}$ and $C_{1\mathrm{b}}$, respectively.

2 Photon shell game Wigner tomography

In order to unambiguously verify the high transfer fidelity of a one-photon Fock state from resonator $\mathrm{R_a}$ to resonator $\mathrm{R_c}$ via resonator $\mathrm{R_b}$, we have performed full-state Wigner tomography on $\mathrm{R_a}$ and $\mathrm{R_c}$ for the two prototypical examples of photon shell game of Fig. 2b(ii),(iv) (cf. main text). The results are displayed in Fig. S. 2, which shows the measured Wigner functions $W(\alpha)$ and corresponding density matrices $\hat{\rho}$ for the Fock state $|1\rangle$ stored first in $\mathrm{R_a}$ and then in $\mathrm{R_c}$ after transfer via $\mathrm{R_b}$.

The Wigner function is obtained as explained in Ref. 1. The resonator is first prepared in the desired microwave photon state $|\Psi\rangle$. Next the resonator is displaced by injecting a coherent state $|-\alpha\rangle$ with complex amplitude $\alpha = |\alpha| \exp(\varphi_\alpha)$, where $|\alpha|$ represents the coherent state real amplitude and φ_α its phase; the state is injected through a microwave control line using a classical pulsed microwave source (cf. Fig. 1a,b in main text). A qubit in its energy ground state is then brought into resonance with the resonator for a variable interaction time, long enough to execute several qubit-resonator swaps. A least-squares fit of the time-dependent oscillations in the qubit energy excited state probability allows

DOI: 10.1038/NPHYS1885

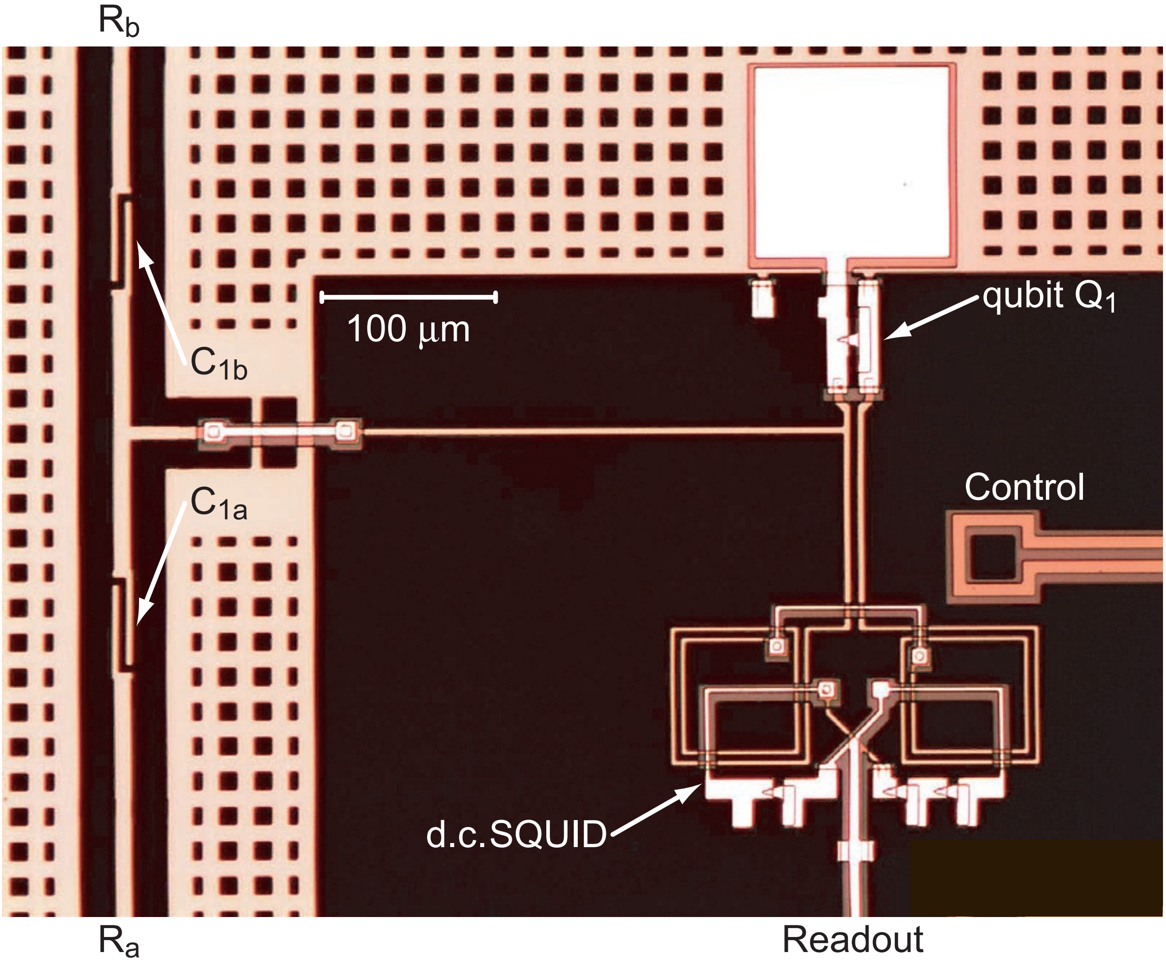

Figure 1: **Detail of qubit Q_1 coupled to resonators R_a and R_b.** The capacitors C_{1a} and C_{1b} couple qubit Q_1 (gradiometer design) to resonators R_a and R_b. The qubit state is read out by a d.c. SQUID (also gradiometer design). A portion of the control and readout lines is also visible. A micrometer scale shows the circuit dimensions.

extraction of the resonator photon number states making up $|\Psi\rangle$, from which the state quasi-probability distributions can be calculated via the parity operator, giving access to full-state Wigner tomography[1–4]. The amplitude and phase of the coherent state used to displace the resonator are calibrated as explained in Ref. 1. From the Wigner function it is possible to reconstruct the density matrix of the resonator state[5] $|\Psi\rangle$.

Given the theoretical $\hat{\rho}_{\rm th}$ and measured $\hat{\rho}_{\rm m}$ density matrices of a resonator state $|\Psi\rangle$, we define the state fidelity as $\mathcal{F} \equiv \mathrm{Tr}\{\hat{\rho}_{\rm th}\,\hat{\rho}_{\rm m}\}$. For the Fock state $|1\rangle$ prepared in R_a, with the measured Wigner function and density matrix shown in Fig. S. 2a,c, we find $\mathcal{F} \simeq 0.84$. This compares well with the fit amplitude to the qubit-resonator swaps, which gives a fidelity $\mathcal{F} \simeq 0.86$ (cf. Fig. 2 in main text). After being transferred to R_c, the state is characterized by the Wigner function and density matrix displayed in Fig. S. 2b,d, with fidelity $\mathcal{F} \simeq 0.64$, which is also consistent with the fidelity $\mathcal{F} \simeq 0.69$ found with a least-squares fit (cf. Fig. 2 in main text). The loss of fidelity occurring during the photon transfer between the three resonators can be attributed to qubit decoherence, due to the qubits crossing spurious two-level systems (TLSs) and due to slight calibration errors during the swap qubit-resonator operations. Nevertheless, it is remarkable that the density matrix associated with the state in R_c is still very pure, with nearly negligible spurious matrix elements and only a small contribution from the $|0\rangle$ state.

3 Harmonic purity and $\sqrt{2}$ scaling for the quantum 'Towers of Hanoi'

Two other figures of merit for the transfer of one- and two-photon Fock states between resonators R_a, R_b and R_c are represented by the harmonic purity of the state (i.e. absence of beatings) and the

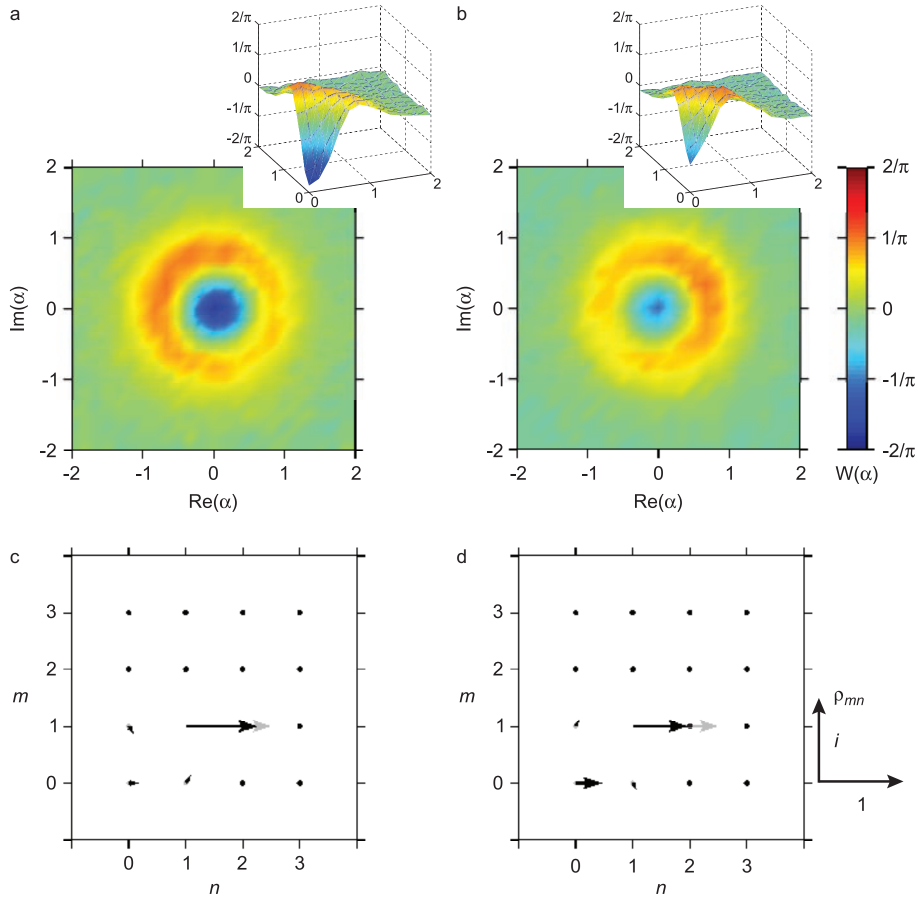

Figure Supplementary 2: **Wigner tomography for the photon shell game. a,** Measured Wigner function $W(\alpha)$ for resonator R_a as a function of the complex resonator amplitude α in square root of photon number units (colour scale bar on the far right). The inset displays a cut of the three-dimensional plot of the Wigner function. **b,** Same as in **a**, but for resonator R_c (colour scale bar on the right). Negative quasi-probabilities clearly indicate the quantum-mechanical nature of the intra-resonator states. **c,** Theoretical (grey) and measured (black) values for the density matrix associated with the state stored in resonator R_a, $\hat{\rho}$, projected onto the number states $\rho_{mn} \equiv \langle m|\hat{\rho}|n\rangle$. The magnitude and phase of ρ_{mn} is represented by the length and direction of an arrow in the complex plane (the scale for the real and imaginary part is reported on the far right). **d,** Same as in **c**, but for resonator R_c. When representing the density matrices, the resonator Hilbert space has been truncated to the lowest four bosonic states.

$\sqrt{2}$ scaling factor between the swap rates for $|1\rangle$ and $|2\rangle$ Fock states[6]. Such figures of merit can be estimated by computing the fast Fourier transform (FFT) of the qubit-resonator vacuum Rabi swaps. Figure Supplementary 3 shows the FFTs for the key steps of the photon shell game and 'Towers of Hanoi', i.e. for a one-photon Fock state $|1\rangle$ and a two-photon Fock state $|2\rangle$ created in R_a and measured with Q_1, then transferred to R_b and measured both with Q_1 and Q_2, and finally transferred to R_c and measured with Q_2. The time-domain swaps used to compute the FFTs are shown in Figs. 2b and 3a in the main text. Figure Supplementary 3 clearly demonstrates the harmonic purity of the states before and after the transfers.

4 Phase coherent transfer

The photon shell game and quantum 'Towers of Hanoi' show that the *populations*, i.e. the diagonal terms of the density matrix, of the one- and two-photon Fock states $|1\rangle$ and $|2\rangle$ can be transferred among resonators with high fidelity. We now turn to the more subtle question whether the *coherences*, i.e. the amplitudes and phases of the off-diagonal terms of the density matrix, are also preserved during a transfer. In order to demonstrate a phase coherent transfer, we synthesized superposition states of the form $|\psi_\varphi\rangle = |0\rangle + e^{i\varphi}|1\rangle$. Such states represent a paradigmatic example of "phase sensitive" state owing

 DOI: 10.1038/NPHYS1885

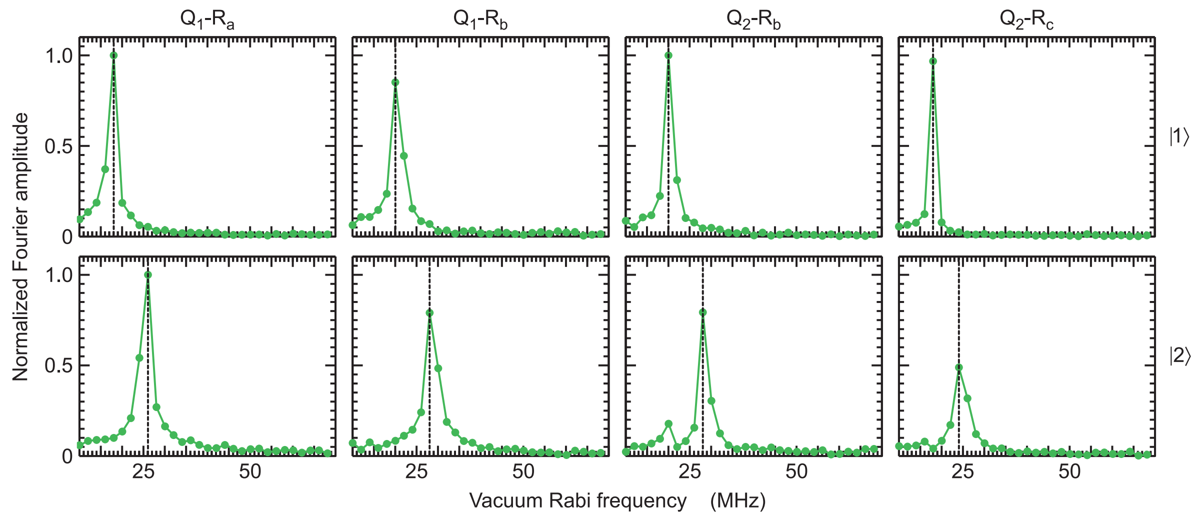

Figure Supplementary 3: **Fourier analysis for the photon shell game and 'Towers of Hanoi'.** Top sub-panels, normalized Fourier amplitude as a function of vacuum Rabi frequency associated with the qubit-resonator Rabi swaps for a one-photon Fock state $|1\rangle$. Bottom sub-panels, normalized Fourier amplitude for a two-photon Fock state $|2\rangle$. Above each column is indicated the respective qubit-resonator interaction. The dashed black line in each sub-panel indicates the maximum Fourier component. The amplitude re-normalization is calculated with respect to the largest Fourier component for Fock state $|1\rangle$ (top sub-panels) and $|2\rangle$ (bottom sub-panels), respectively. The $\sqrt{2}$ scaling[1] between the $|1\rangle$ and $|2\rangle$ states is clearly visible. The absence of beatings (only a small beating, owing to some residual presence of state $|1\rangle$, for state $|2\rangle$ in the Q_2-R_b sub-panel) shows the high level of harmonic purity of the states transferred between the three resonators, both for the photon shell game and for the more complex 'Towers of Hanoi'.

to the presence of non-zero off-diagonal terms in the density matrix, which reads

$$\hat{\rho}_\varphi = \frac{1}{2}\begin{bmatrix} 1 & e^{-i\varphi} \\ e^{+i\varphi} & 1 \end{bmatrix}. \tag{S-1}$$

In particular we have synthesized two orthogonal superposition states $|\psi_X\rangle = |0\rangle + e^{i\varphi_X}|1\rangle$ and $|\psi_Y\rangle = |0\rangle + e^{i\varphi_Y}|1\rangle$, where the respective phases differ by $\pi/2$, $\varphi_Y - \varphi_X = \pi/2$.

The main steps of these phase-coherent transfer experiments, the results of which are shown in Fig. 3b,c in the main text, are as follows:

1. Qubit Q_1 is initialized in the energy ground state $|\mathrm{g}\rangle$ by letting it relax for a time much longer than its energy relaxation time T_1^{rel}. The qubit idle point is chosen to be in-between, and well away from, the transition frequencies of resonators R_a and R_b;

2. A Gaussian-shape $\pi/2$-pulse with a full width at half maximum of 7 ns and phase φ_X or φ_Y is applied to Q_1 in order to prepare the qubit in state $|\mathrm{g}\rangle + e^{i\varphi_X}|\mathrm{e}\rangle$ or $|\mathrm{g}\rangle + e^{i\varphi_Y}|\mathrm{e}\rangle$;

3. At the end of the $\pi/2$-pulse, a z-pulse is applied to Q_1, which brings the qubit into resonance with resonator R_a for a swap time[8] $1/2g_{1a} \simeq 27.68$ ns. This swap operation maps the state in Q_1 into R_a, which is thus left in state $|0\rangle + e^{i(\varphi_X + \delta\varphi_{1a})}|1\rangle$ or in the orthogonal state $|0\rangle + e^{i(\varphi_Y + \delta\varphi_{1a})}|1\rangle$. Here, the phase $\delta\varphi_{1a}$ is the dynamic phase accumulated during the z-pulse/swap operation. The phase φ_X of the $\pi/2$-pulse is chosen to compensate the dynamic phase $\delta\varphi_{1a}$, so that $\varphi_X^{\mathrm{st}} = \varphi_X + \delta\varphi_{1a} = 0$. In this manner, R_a is effectively prepared in state $|\psi_X\rangle = |0\rangle + |1\rangle$, where all terms of the density matrix should be purely real, or in the orthogonal state $|\psi_Y\rangle = |0\rangle + e^{i\pi/2}|1\rangle$. As an important check $|\psi_X\rangle$ and $|\psi_Y\rangle$ should remain orthogonal before and after transfer between different resonators;

4. Implementing the tomography technique described in Ref. 9, we measure the density matrix of the states synthesized in R_a and deduce the corresponding Wigner function. The top and bottom panels to the left in Fig. 3b in the main text show the resulting density matrices for state $|\psi_X\rangle$ and $|\psi_Y\rangle$, respectively. The corresponding Wigner functions are shown in the top and bottom panels to the left in Fig. 3c in the main text. The state fidelity for $|\psi_X\rangle$ is $\simeq 0.91$ and for $|\psi_Y\rangle$ is $\simeq 0.92$. Owing to a slight miscalibration of the $\pi/2$-pulse and/or swap time into R_a, the off-diagonal terms (red arrows in Fig. 3b in the main text) of the density matrix of $|\psi_X\rangle$ are tilted by an angle

Table Supplementary 1: **Density matrix elements for $|\psi_X\rangle$ and $|\psi_Y\rangle$.** Density matrices and corresponding Wigner functions are shown in Fig. 3b,c (cf. main text). Only the elements for $m, n = 0, 1$ are reported here. The sample used for these experiments differs from those used in the rest of the paper and is characterized by a higher density of strongly coupled TLSs; the loss of population ($\langle 1|\hat{\rho}|1\rangle$ element) in the preparation and transfer of each state is due to these TLSs. Remarkably, the coherences ($\langle 0|\hat{\rho}|1\rangle \equiv \langle 1|\hat{\rho}|0\rangle^*$ elements) are only marginally affected by the TLSs.

	$\langle 0\|\hat{\rho}\|0\rangle$	$\langle 0\|\hat{\rho}\|1\rangle \equiv \langle 1\|\hat{\rho}\|0\rangle^*$	$\langle 1\|\hat{\rho}\|1\rangle$
$\|\psi_X\rangle$ in $\mathrm{R_a}$	0.63	0.43+0.03i	0.33
$\|\psi_Y\rangle$ in $\mathrm{R_a}$	0.61	0.04-0.44i	0.35
$\|\psi_X\rangle$ in $\mathrm{R_b}$	0.87	0-0.14i	0.02
$\|\psi_Y\rangle$ in $\mathrm{R_b}$	0.86	-0.08-0.15i	0.03
$\|\psi_X\rangle$ back in $\mathrm{R_a}$	0.68	0.38+0.05i	0.24
$\|\psi_Y\rangle$ back in $\mathrm{R_a}$	0.71	0.07-0.36i	0.20

$|\varphi_X^{\mathrm{st}}| \simeq 4.30°$ and those of $|\psi_Y\rangle$ by an angle $|\varphi_Y^{\mathrm{st}}| \simeq 4.75°$. Defining the orthogonality between $|\psi_X\rangle$ and $|\psi_Y\rangle$ as $X \perp Y \equiv |(90° - |\varphi_Y^{\mathrm{st}}|) - (0° - |\varphi_X^{\mathrm{st}}|)|/90°$, we obtain $X \perp Y^{\mathrm{st}} \simeq 0.995$;

5. The states $|\psi_X\rangle$ and $|\psi_Y\rangle$ are then transferred to $\mathrm{R_b}$ by bringing $\mathrm{Q_1}$ again into resonance with $\mathrm{R_a}$ for a swap time $1/2g_{1\mathrm{a}}$ and subsequently into resonance with $\mathrm{R_b}$ for a swap time $1/2g_{1\mathrm{b}} \simeq 23.89$ ns. We then measure again the density matrix for $\mathrm{R_a}$ to show that the resonator is left in the vacuum state. The top and bottom panels in the middle of Fig. 3b in the main text show the resulting density matrices for the resonator state after $|\psi_X\rangle$ and $|\psi_Y\rangle$ have been shuffled to $\mathrm{R_b}$. The corresponding Wigner functions are shown in the top and bottom panels in the middle of Fig. 3c in the main text. The density matrices and Wigner functions clearly show that the resonator is now in the vacuum state $|0\rangle$, with state fidelity $\simeq 0.87$ in the $|\psi_X\rangle$ case and $\simeq 0.86$ in the $|\psi_Y\rangle$ case;

6. After storing $|\psi_X\rangle$ and $|\psi_Y\rangle$ in $\mathrm{R_b}$ for a few nanoseconds, $\mathrm{Q_1}$ is brought into resonance with $\mathrm{R_b}$ for the usual swap time $1/2g_{1\mathrm{b}}$ and finally into resonance with $\mathrm{R_a}$ for a swap time $1/2g_{1\mathrm{a}}$. At the end of this last swap, $|\psi_X\rangle$ and $|\psi_Y\rangle$ are back in $\mathrm{R_a}$, accompanied by a total dynamic phase that depends on the qubit detunings from the idle point and duration of the various z-pulse/swap operations. It is only by coincidence that the dynamic phase in the experiments reported in the main text happens to be close to 2π and, thus, the off-diagonal terms of the density matrix and the Wigner function shown in the top panel to the right in Fig. 3b,c in the main text display a similar angle as those in the top panel to the left in Fig. 3b,c (a similar argument applies to the matrices and Wigner functions in the bottom panels to the left and right in Fig. 3b,c). In general, the total dynamic phase accumulated during the transfer from $\mathrm{R_a}$ to $\mathrm{R_b}$ will have an arbitrary value. Consequently, the critical check to assure that timing errors in the pulse sequence do not compromise the integrity of the off-diagonal terms of the density matrices is to compare the orthogonality between $|\psi_X\rangle$ and $|\psi_Y\rangle$ before and after the transfer. The orthogonality after the transfer to $\mathrm{R_b}$ is $X \perp Y^{\mathrm{fin}} \simeq 0.958$. The overall transfer orthogonality is then given by $(X \perp Y^{\mathrm{fin}})/(X \perp Y^{\mathrm{st}}) \simeq 0.963$. This result demonstrates a high fidelity phase coherent transfer of photonic states between the two resonators. In addition to a good orthogonality, we also note that the state fidelities for $|\psi_X\rangle$ and $|\psi_Y\rangle$ in $\mathrm{R_a}$ after transfer through $\mathrm{R_b}$ are $\simeq 0.84$ and $\simeq 0.81$, respectively, which compare well to the state fidelities for a $|0\rangle + |1\rangle$ state generated in a single resonator architecture (cf. Ref. 1). The overall transfer fidelity given by the ratio between the state fidelity after and before the transfer is $\simeq 0.92$ and $\simeq 0.88$ for $|\psi_X\rangle$ and $|\psi_Y\rangle$, respectively.

Table Supplementary 1 shows the density matrix elements for state $|\psi_X\rangle$ and $|\psi_Y\rangle$ at the various stages of the shell game between resonators $\mathrm{R_a}$ and $\mathrm{R_b}$.

5 Energy relaxation model of the two-resonator vacuum Rabi swaps

We next discuss the energy relaxation mechanism of the two-resonator vacuum Rabi swaps shown in Fig. 5d of the main text. The decay times for qubit $\mathrm{Q_1}$ and resonators $\mathrm{R_a}$ and $\mathrm{R_b}$ are shown in Fig. S. 4. The resonators' energy relaxation time is determined by preparing a one-photon Fock state $|1\rangle$ in the resonator, storing it for a variable time, and then measuring by bringing a qubit on resonance with

DOI: 10.1038/NPHYS1885

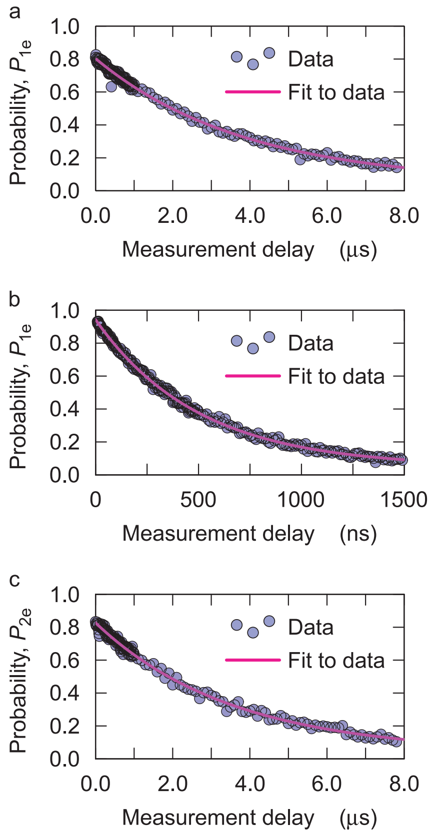

Figure Supplementary 4: **Energy relaxation for qubit Q_1 and resonators R_a and R_b**. In all panels: P_{pe} is the probability to find Q_p in $|e\rangle$ as a function of measurement delay time (i.e. the time an excitation is stored in a resonator or qubit before readout). Full circles are data and solid magenta lines exponential fits to data. **a,** Measurement of the energy relaxation of resonator R_a using qubit Q_1 as a detector[10,11]. **b,** Energy relaxation of qubit Q_1. **c,** Same as in **a**, but for resonator R_b.

the resonator, swapping the state into the qubit, and finally reading out the qubit state. The energy relaxation times are obtained from a simple exponential fit, as reported in Table Supplementary 2. The qubit and resonator energy relaxation times, as well as the other parameters listed in that table, are used to numerically solve a Lindblad-type master equation[13,14]:

$$\dot{\hat{\rho}} = \frac{1}{i\hbar}(\widehat{H}_1\hat{\rho} - \hat{\rho}\widehat{H}_1) + \sum_{k=1}^{3} \hat{\mathcal{L}}_k\,\hat{\rho}\,, \tag{S-2}$$

where $\hat{\rho}$ is the total density matrix of the system, $\dot{\hat{\rho}} \equiv (\partial/\partial t)\,\hat{\rho}$ its time derivative, $\widehat{H}_1$ is the Hamiltonian of Eq. (1) (cf. Methods' section in main text), $\hat{\mathcal{L}}_k$ is the Lindblad superoperator defined as $\hat{\mathcal{L}}_k\,\hat{\rho} \equiv \gamma_k(\widehat{X}_k\hat{\rho}\widehat{X}_k^\dagger - \widehat{X}_k^\dagger\widehat{X}_k\,\hat{\rho}/2 - \hat{\rho}\,\widehat{X}_k^\dagger\widehat{X}_k/2)$ and $k \in \mathbb{N}$. The qubit and resonator decay rates are defined as $\gamma_1 \equiv 1/T_{\mathrm{a}}^{\mathrm{rel}}$, $\gamma_2 \equiv 1/T_1^{\mathrm{rel}}$ and $\gamma_3 \equiv 1/T_{\mathrm{b}}^{\mathrm{rel}}$ and the generating operators as $\widehat{X}_1 \equiv \hat{a}$, $\widehat{X}_1^\dagger \equiv \hat{a}^\dagger$, $\widehat{X}_2 \equiv \hat{\sigma}^-$, $\widehat{X}_2^\dagger \equiv \hat{\sigma}^+$, $\widehat{X}_3 \equiv \hat{b}$ and $\widehat{X}_3^\dagger \equiv \hat{b}^\dagger$. We numerically solve Eq. (S-2) for the pulse sequence shown in Fig. 5a (cf. main text), without accounting for the measurement process. The results are displayed in Fig. S. 5, compared to the experimental data.

Figure Supplementary 5a,c shows the same data as in Fig. 5d (cf. main text), but for a transfer time τ that is three times longer. The data shown in Fig. S. 5a,c were taken using a different device than Fig. 5d, with longer qubit relaxation times. The exponential decay obtained by the simple harmonic mean model (cf. main text) is superposed with the data, making evident the qualitative validity of the model. Figure Supplementary 5b,d show the results of the numerical simulations of Eq. (S-2) corresponding to the experimental data of Fig. S. 5a,c, respectively, with the amplitude of the simulations adjusted to match the measured amplitudes. Data and simulations are in very good agreement, supporting the simple harmonic mean decay model. In particular, the experimental decay time obtained by fitting the data is $\simeq 840$ ns, from simulations $\simeq 874$ ns and from the harmonic mean model $\simeq 896$ ns. The slight

DOI: 10.1038/NPHYS1885

Table Supplementary 2: **Parameters for numerical simulations of two-resonator vacuum Rabi swaps.** δ is the qubit non-linearity, i.e. the frequency difference between the qubit ground-to-first excited state transition relative to the first-to-second excited state transition [12]. The non-linearity has been used in the simulations to take into account possible leakage outside of the qubit subspace. T_{a}^{ϕ} and T_{b}^{ϕ} are the dephasing times for resonators $\mathrm{R_a}$ and $\mathrm{R_b}$, respectively. Since we want to study the energy relaxation of the two-resonator Rabi swaps, the qubit dephasing time T_1^{ϕ} has been neglected in the simulations. All the other parameters are defined in the main text.

$\mathbf{R_a}$	f_{a} (GHz)	–	$g_{1\mathrm{a}}$ (MHz)	$T_{\mathrm{a}}^{\mathrm{rel}}$ (ns)	T_{a}^{ϕ} (ns)
	6.340		17.95	3881	$\gg T_{\mathrm{a}}^{\mathrm{rel}}$
$\mathbf{Q}_1$	f_1 (GHz)	δ (MHz)	–	T_1^{rel} (ns)	T_1^{ϕ} (ns)
	6.563	204.23		507	––
$\mathbf{R_b}$	f_{b} (GHz)	–	$g_{1\mathrm{b}}$ (MHz)	$T_{\mathrm{b}}^{\mathrm{rel}}$ (ns)	T_{b}^{ϕ} (ns)
	6.815		20.25	3549	$\gg T_{\mathrm{b}}^{\mathrm{rel}}$

discrepancy between the experimental data and simulations for the low occupation probabilities (causing an offset between data and simulations) is because the simulations do not account for the measurement process. Note that we can safely assume that only qubit $\mathrm{Q_1}$ and resonator $\mathrm{R_a}$, swapping for a variable transfer time τ, contribute to the effective decay mechanism of the two-resonator Rabi dynamics. In fact, the second resonator serves only as a mapping resonator, the state of which is measured with $\mathrm{Q_2}$ typically after a time $\Delta\tau_2 \ll T_{\mathrm{b}}^{\mathrm{rel}}$ (cf. Fig. 5b,c in main text). In other words, examining the two-dimensional plots of Fig. 5b,c we expect two distinct decay mechanisms. The first along the horizontal axis ($\Delta\tau_1$ and $\Delta\tau_2$). This decay is practically negligible as this measurement is completed in $\leqslant 30\,\mathrm{ns}$. The second is along the vertical axis (τ) related to the $\mathrm{Q_1}$-$\mathrm{R_a}$ swaps, as explained above. A theoretical analysis of the decay mechanisms characteristic for two-resonator dynamics in different regimes may be found in Ref. 15.

DOI: 10.1038/NPHYS1885

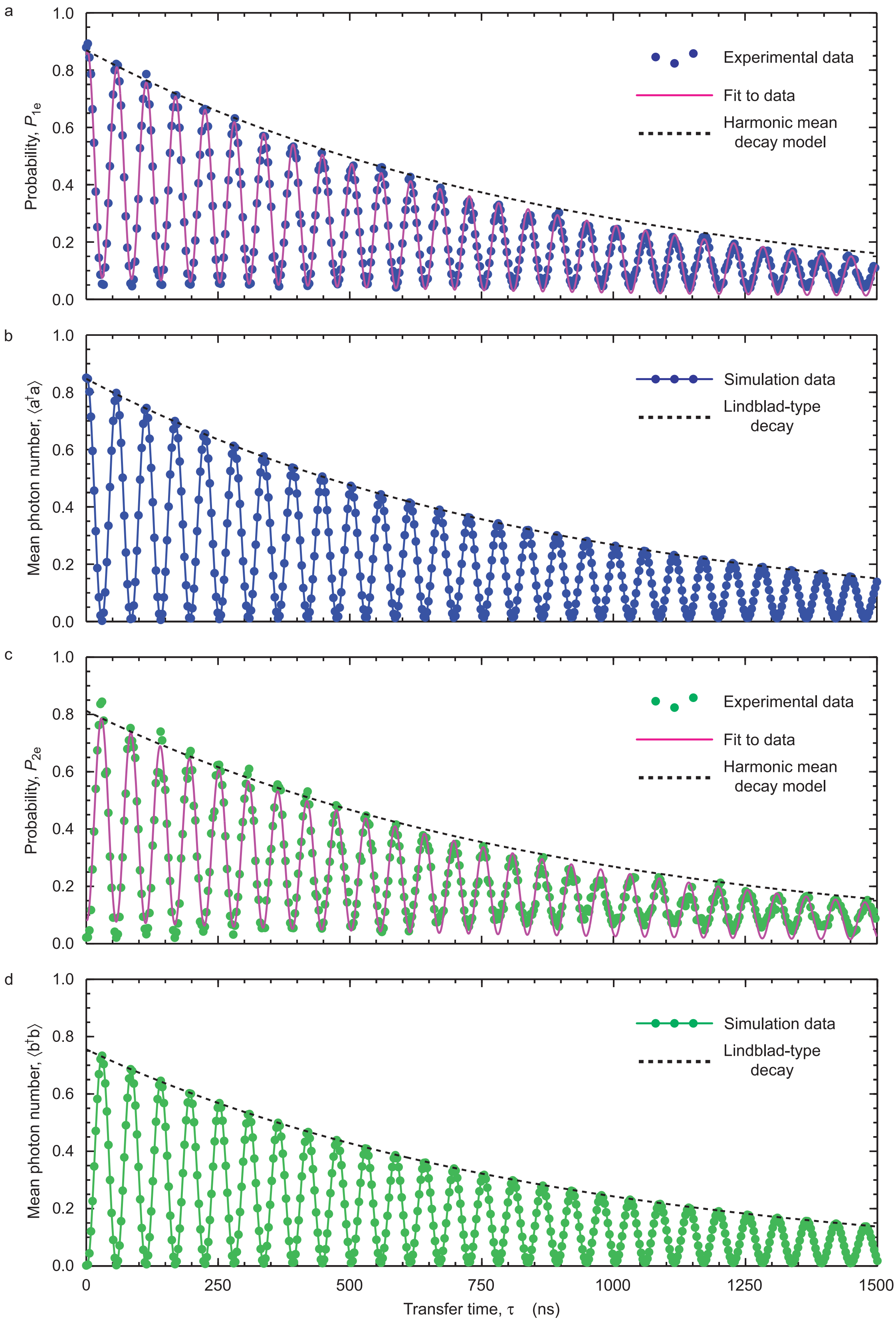

Figure Supplementary 5: **Numerical simulations of two-resonator Rabi swaps. a,** $\mathrm{R_a}$ state dynamics measured as the probability $P_{1\mathrm{e}}$ to find $\mathrm{Q_1}$ in $|\mathrm{e}\rangle$ vs. time τ. Dark blue circles are data, solid magenta line a least-squares fit to data and dashed black line the exponential harmonic mean decay. **b,** Simulation of the data in **a**, showing the resonator mean photon number $\langle \hat{a}^\dagger \hat{a} \rangle$ vs. τ. **c,** Same as in **a**, but for $\mathrm{R_b}$. Light green circles are data, solid magenta line a least-squares fit to data and dashed black line the exponential harmonic mean decay. **d,** Same as in **b**, but for $\mathrm{R_b}$.

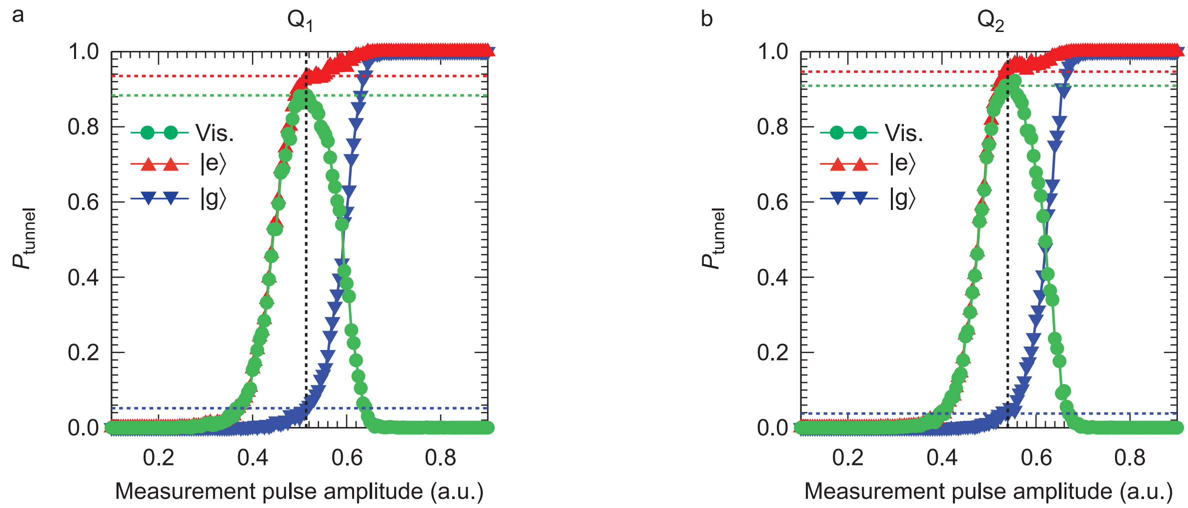

Figure Supplementary 6: **"S-curve" calibrations for qubit Q_1 and Q_2. a,** Dark blue down triangles connected by a dark blue solid line: Tunnel probability as a function of measurement pulse amplitude for Q_1 in the energy ground state $|g\rangle$. Red up triangles connected by a red solid line: Tunnel probability as a function of measurement pulse amplitude for Q_1 in the energy excited state $|e\rangle$. Light green circles connected by a light green solid line: Visibility curve for Q_1 obtained subtracting the S-curves for Q_1 in $|g\rangle$ and $|e\rangle$, respectively. The vertical dashed black line indicates the amplitude of the measurement pulse set in the experiments described in the paper. The dark blue, light green and red horizontal dashed lines (bottom to top) indicate the ground state measurement error E_g, the qubit visibility V and the excited state measurement fidelity F_e, respectively. **b,** Same as in **a**, but for qubit Q_2.

6 Correction for measurement errors

The data shown in the main text and here have been corrected for measurement errors, following the procedure outlined in Ref. 16. This consists in performing a so-called "S-curve" calibration, where the amplitude of the qubit measurement pulse is swept while the probability of the qubit tunneling out of the metastable well (where the ground and excited qubit states $|g\rangle$ and $|e\rangle$ are confined) is measured. The tunneling rate is lower for $|g\rangle$ than for $|e\rangle$, allowing the two states to be discriminated. A tunneling event is easily detected by means of the d.c. SQUID lithographically defined adjacent to each qubit (cf. Fig. S. 1).

The S-curve calibrations for qubit Q_1 and Q_2 are shown in Fig. S. 6a,b, with the probability of tunneling plotted versus the measurement pulse amplitude. In the experiments, the amplitude of the measurement pulse was set to the value indicated by the vertical dashed black line. This gives the probability of tunneling for a $|g\rangle$ state close to $\simeq 0.05$, which we term the *ground state measurement error* E_g. For the same measurement pulse amplitude, the probability for the $|e\rangle$ state to tunnel, which we term the *excited state measurement fidelity* F_e, is close to unity. The *qubit visibility* is defined as the difference $V = F_e - E_g$. For qubit Q_1 we find $E_g \simeq 0.052$, $F_e \simeq 0.935$ and $V = 0.883$. For qubit Q_2 we find $E_g \simeq 0.038$, $F_e \simeq 0.947$ and $V = 0.909$.

The correction for measurement errors is realized by re-scaling any measured excited state probability P_e to $\widetilde{P}_e$ according to

$$\widetilde{P}_e = \frac{P_e - E_g}{V}\,.$$

Given the good visibility of the qubits this correction is relatively small. We note that some of the experiments reported here were performed with different devices characterized by slightly different visibilities, but in all cases V was very close to 0.9.

DOI: 10.1038/NPHYS1885

References

1. Hofheinz, M., Wang, H., Ansmann, M., Bialczak, R. C., Lucero, E., Neeley, M., O'Connell, A. D., Sank, D., Wenner, J., Martinis, J. M. & Cleland, A. N. Synthesizing arbitrary quantum states in a superconducting resonator. *Nature (London)* **459**, 546–549 (2009).

2. Haroche, S. & Raimond, J.-M. *Exploring the quantum.* (Oxford University Press Inc., New York, 2006).

3. Leonhardt, U. *Measuring the quantum state of light.* (Cambridge University Press, Cambridge, 1997).

4. Bertet, P., Auffeves, A., Maioli, P., Osnaghi, S., Meunier, T., Brune, M., Raimond, J.-M. & Haroche, S. Direct measurement of the Wigner function of a one-photon Fock state in a cavity. *Phys. Rev. Lett.* **89**, 200402 (2002).

5. Leibfried, D., Meekhof, D. M., King, B. E., Monroe, C., Itano, W. M. & Wineland, D. J. Experimental determination of the motional quantum state of a trapped atom. *Phys. Rev. Lett.* **77**, 4281-4285 (1996).

6. Hofheinz, M., Weig, E. M., Ansmann, M., Bialczak, R. C., Lucero, E., Neeley, M., O'Connell, A. D., Wang, H., Martinis, J. M. & Cleland, A. N. Generation of Fock states in a superconducting quantum circuit. *Nature (London)* **454**, 310–314 (2008).

7. Note that, as a convention, we usually did not normalize quantum states. We however use the appropriate normalization factor of 1/2 for the density matrix of Eq. S-1 for better comparison between theory and data.

8. Note that the coupling strengths and corresponding swap times in this specific experiment are slightly different than in the shell game and 'Towers of Hanoi' described in the main text becasue of a different sample.

9. Wang, H., Hofheinz, M., Ansmann, M., Bialczak, R. C. Lucero, E., Neeley, M., O'Connell, A. D., Sank, D., Weides, M., Wenner, J., Cleland, A. N. & Martinis, J. M. Decoherence dynamics of complex photon states in a superconducting circuit. *Phys. Rev. Lett.* **103**, 200404 (2009).

10. Neeley, M., Ansmann, M., Bialczak, R. C., Hofheinz, M., Katz, N., Lucero, E., O'Connell, A., Wang, H., Cleland, A. N. & Martinis, J. M. Process tomography of quantum memory in a Josephson-phase qubit coupled to a two-level state. *Nature Physics* **4**, 523–526 (2008).

11. Wang, H., Hofheinz, M., Ansmann, M., Bialczak, R. C., Lucero, E., Neeley, M., O'Connell, A. D., Sank, D., Wenner, J., Cleland, A. N. & Martinis, J. M. Measurement of the decay of Fock states in a superconducting quantum circuit. *Phys. Rev. Lett.* **101**, 240401 (2008).

12. Lucero, E., Kelly, J., Bialczak, R. C., Lenander, M., Mariantoni, M., Neeley, M., O'Connell, A. D., Sank, D., Wang, H., Weides, M., Wenner, J., Yamamoto, T., Cleland, A. N. & Martinis, J. M. Reduced phase error through optimized control of a superconducting qubit. *Phys. Rev. A* **82**, 042339 (2010).

13. Walls, D. F. & Milburn, G. J. *Quantum optics* 2nd ed. (Springer-Verlag, Berlin-Heidelberg, 2008).

14. Blais, A., Huang, R.-S., Wallraff, A., Girvin, S. M. & Schoelkopf, R. J. Cavity quantum electrodynamics for superconducting electrical circuits: an architecture for quantum computation. *Phys. Rev. A* **69**, 062320 (2004).

15. Reuther, G. M., Zueco, D., Deppe, F., Hoffmann, E., Menzel, E. P., Weißl, T., Mariantoni, M., Kohler, S., Marx, A., Solano, E., Gross, R., & Hänggi, P. Two-resonator circuit quantum electrodynamics: dissipative theory. *Phys. Rev. B* **81**, 144510 (2010).

16. Ansmann, M., Wang, H., Bialczak, R. C., Hofheinz, M., Lucero, E., Neeley, M., O'Connell, A. D., Sank, D., Weides, M., Wenner, J., Cleland, A. N. & Martinis, J. M. Violation of Bell's inequality in Josephson phase qubits. *Nature (London)* **461**, 504–506 (2009).